JOURNAL OF MATERIALS SCIENCE **39** (2004) 5701 – 5709

Microstructural dependence of giant-magnetoresistance in electrodeposited Cu-Co alloys

T. COHEN-HYAMS
Department of Materials Engineering, Technion, Haifa, Israel
E-mail: mtcohen@tx.technion.ac.il

J. M. PLITZKO
Department of Molecular Structural Biology, Max-Planck-Institute of Biochemistry, Germany

C. J. D. HETHERINGTON, J. L. HUTCHISON
Department of Materials, Oxford University, UK

J. YAHALOM, W. D. KAPLAN
Department of Materials Engineering, Technion, Haifa, Israel

The relationship between the microstructure and the magnetic properties of heterogeneous Cu-Co [Cu92.5-Co7.5] (at.%) thin films prepared by electrodeposition was studied. Electron spectroscopic imaging (ESI) studies clearly revealed the evolution of the cobalt microstructure as a function of thermal treatments. The as-deposited film is composed of more than one phase; metastable Cu-Co, copper and cobalt. During annealing the metastable phase decomposes into two fcc phases; Cu and Co. Grain growth occurs with increasing annealing duration, such that the cobalt grains are more homogeneously distributed in the copper matrix. A maximum GMR effect was found after annealing at 450°C for 1.5 h, which corresponds to an average cobalt grain size of 5.5 nm according to magnetization characterization. A significant fraction of the cobalt in the Cu-Co film did not contribute to the GMR effect, due to interactions between the different magnetic grains and large ferromagnetic (FM) grains. The percolation threshold of cobalt in metastable Cu-Co alloys formed by electrodeposition is lower (less than ∼7.5 at.%) than that prepared by physical deposition methods (∼35 at.%).

1. Introduction

The giant magnetoresistance (GMR) effect, which was first discovered in magnetic multilayers [1] also exists in heterogeneous alloys with ferromagnetic granules (i.e., Fe or Co) embedded in a non-magnetic metal (i.e., Cu or Ag) [2–5]. GMR refers to a significant change in the electrical resistance of a film or a device when an external magnetic field is applied. Heterogeneous alloy films are immiscible combinations usually prepared by physical deposition methods [6, 7] and by electrodeposition [8–17], which are subsequently heat treated causing the precipitation of small ferromagnetic particles in a medium of a non-magnetic matrix. In heterogeneous systems, the ferromagnetic grains are distributed within a nonmagnetic matrix, where the GMR effect mainly originates from spin-dependent scattering of conduction electrons at the interface of the ferromagnetic (FM) particles [18]. Therefore, the microstructural factors controlling the magnetization and the GMR effect in granular materials are expected to be the grain size of the ferromagnetic phase, size distribution, shape and the volume fraction of the ferromagnetic phase embedded in the non-ferromagnetic matrix, the amount of superparamagnetic (SM) particles as well as the roughness of the interface [3, 4, 6].

A characteristic heterogeneous alloy, which presents high values of GMR, is the Cu-Co alloy [2]. This system is immiscible at room temperature, and the formation of a supersaturated Cu-Co phase is possible [19]. Subsequent annealing causes cobalt precipitation in a non-magnetic matrix (Cu) and a heterogeneous microstructure is formed. The magnetic properties and GMR effect of different compositions of Cu-Co alloys formed by different techniques have been extensively studied [5–7, 9–11, 13, 15]. The Cu-Co alloys were characterized mainly by X-ray diffraction (XRD) [5, 10, 11, 13, 15, 16, 18] and by transmission electron microscopy (TEM) [5, 6, 14, 15, 18, 20–29]. Wang *et al.* [24] and Yang *et al.* [25] performed HRTEM combined with energy dispersive spectroscopy (EDS) analysis on Cu-Co alloys formed by melt spinning and observed a few Co grains. However, a clear profile of the as-deposited FM grain size and shape distribution, and its dependence on annealing is not clear.

In addition, a contradiction between the XRD characterization and the magnetic results is reported in the literature [5, 10, 11, 13–15, 23, 28, 29]. According to the XRD analysis the as-deposited Cu-Co alloy is a fcc Cu-Co solid solution, but the magnetization results indicated a SP behavior, meaning that the alloy is composed of very small Co grains and that at least some of the cobalt in the alloy is a pure Co phase (fcc or hcp). The absence of an fcc cobalt reflection in the XRD spectrum is probably related to the relatively low content of cobalt (<20 at.%) and to the small grain size of cobalt (nano-scale). It may also indicate the integration of two reflections; (111) fcc Cu with (111) fcc Co or that the Co grains are strained, which may cause a shift in the d-space.

Thus, the relationship between the GMR effect and the cobalt microstructure in the as-deposited Cu-Co films and as a function of thermal treatments has not been elucidated so far, since it is difficult to study the microstructural features in a granular Cu-Co alloy by conventional TEM. This is due to the small difference in the atomic scattering factor between Cu and Co. The use of high-resolution transmission electron microscopy is also limited in this system due to the small lattice mismatch between Cu and α-Co ($(a_{Cu} - a_{Co})/a_{Cu} = 1.68\%$).

Additionally, it is extremely difficult to distinguish sub-nanometer sized particles embedded in a matrix by selected area electron diffraction or nano-diffraction in the TEM.

An approach that overcomes these difficulties is analytical electron microscopy (AEM). Electron spectroscopic imaging (ESI) provides the two-dimensional distribution of elements under investigation. ESI is a very fast and elegant method to determine not only the location of very small ($\leq$2 nm) precipitates [31], but can also provide qualitative and even quantitative information about intermetallic mixing [32–34].

The aim of the present research is to investigate the relationship of the microstructure with the magnetic properties of electrodeposited Cu-Co.

2. Experimental

Heterogeneous Cu-Co films were electrodeposited with a concentration of 7.5 (at.%) Co. The electrodeposition experiments were conducted on Si wafers, which were previously coated with a PVD copper layer (75 nm) on top of a TaN layer (30 nm). Full details of the electrodeposition process are described in detail elsewhere [35]. The thickness of the Cu-Co films were 1 μm. The samples were deposited at room temperature without agitation, and afterwards were annealed at 450°C for 0.5, 1.5, 10 and 20 h in a reducing atmosphere of Ar + 7%H_2.

2.1. Characterization methods

The microstructural characteristics of the granular Cu-Co films, as-deposited and annealed, were investigated by X-ray diffraction (XRD), scanning Auger microprobe (AES) and energy filtered transmission electron microscopy (EFTEM).

The composition ratio of the Cu-Co alloy was determined by energy dispersive spectroscopy (EDS), using a Pentafet EDS detector and Oxford Link ISIS Software attached to a Philips XL30 scanning electron microscope (SEM), operated at 20 kV at a working distance of 10.5 mm (penetration radius of $\sim$1 μm for Cu K_α at 20 kV). The EDS results were obtained after calibration with a cobalt standard.

The XRD system used in this study (Philips PW-3020 Goniometer) included a long fine-focus copper X-ray tube ($\lambda = 0.15406$ nm), operated routinely at 40 kV and 40 mA with 1° divergent and anti-scattering slits coupled with 0.2 mm receiving slit. A curved graphite monochromator ($2\alpha = 26.4°$) preceded the detector. Diffraction patterns were acquired at steps of 0.02° 2θ and 30 s/step exposures.

The average cobalt grain size was determined based on the Integral Breadth method [36] using XRD reflections. The peak profiles of the XRD reflections were fitted using the pseudo-Voigt function. The FWHM (Full Width of the Half Maximum) and the integral breadth (width of a rectangle with the height of the peak maxima) were extracted using WinFit Beta Release 1.2.1 [37]. The instrumental broadening is determined from XRD profiles of large grained alumina samples and eliminated from the calculations by a simple deconvolution. The average grain size was calculated using a MS-Excel spreadsheet prepared by I.T. Walker [38].

A scanning Auger microprobe (Thermo-VG Scientific Microlab 350) system was used to measure the surface composition and the depth profile of Cu and Co atoms in the Cu-Co film. The incident electron beam energy was 5 keV, the current was 15 nA. Auger transitions of the elements used were: C-KLL-272 eV, N-KLL-390 eV, O-KLL-503 eV, Co-LMM-775 eV, Cu-LMM-918 eV, Si-KLL-1619 eV and Ta-MNN-1675 eV. Ar^+ ions accelerated at 4 kV were used to sputter with an approximate sputter rate of 0.2 nm/s, as estimated from a Ta_2O_5 standard. The incident angles of the Ar^+ bombardment and that of the electron beam relative to the samples were $\sim$48° and 30°, respectively. Depth profiles were obtained by measuring the peak-to-peak areas in the first derivative mode of the corresponding Auger transitions.

TEM samples were prepared using mechanical thinning, dimpling and argon ion-milling. The EFTEM investigations were performed on a Philips CM300 FEG ST and on a Jeol JEM-3000F FEGTEM which were equipped with a Gatan Imaging Filter (GIF) and a 2048 × 2048 CCD camera. The images were acquired using Digital Micrograph 3.3.1. (DM 3.3.1) (additionally customized scripts were used within DM 3.3.1.). The cobalt grain size was measured from EFTEM micrographs using Image Pro Plus 2.0 software.

2.2. Magnetic measurements

The magnetization behavior and magnetoresistivity measurements were performed using an Oxford Teslatron magnetometer. Hysteresis loops were also performed at room temperature (298 K) in a Vibrating Sample Magnetometer (VSM) especially assembled to

TABLE I Summary of cobalt characterization using TEM, XRD and magnetic measurements

Annealing time (h)	D (nm) (TEM)	D (nm) (XRD fcc Co)	SP fraction (%)	D (nm) magnetization	Coercive field (G)	GMR (%) at 5 K
0	<1 nm	0	31	0.83	100	−6
0.5	3.6	3.5	42	1.2	390.7	−12.8
1.5	10	5.8	8	5.5	221.6	−14.6
10	7	35	1	11.7	303.5	−5.6
20	–	31	1	21.6	355	−4

operate at temperatures ranging from 0.5 to 800 K and fields up to 16 T. The magnetic field was perpendicular to the surface of the samples.

Electrical resistivity was measured as a function of magnetic field (H) at 5 and 273 K, using a four-point probe configuration. The measurements were performed with an in-plane DC-current mode using a digital voltmeter. The resistivity measurements were performed with the magnetic field parallel and perpendicular to the sample. The magnetoresistance ratio (MR) was calculated as the fractional change in the zero-field resistance ($R_H = 0$), i.e.,

$$\mathrm{MR}(\%) = 100 \times ((R_H - R_{H=0})/R_{H=0}) \qquad (1)$$

where R_H is the resistance in the presence of a magnetic field H.

3. Results

3.1. XRD

XRD analysis was conducted on samples before and after thermal treatments. The results are given in Fig. 1. The reflections position was calibrated according to the absolute position of Si (400). A full description of the XRD results is published elsewhere [35]. The Cu-Co films exhibited a preferred orientation of (111) planes before and after sequences of thermal treatments. A clear reflection from a fcc cobalt phase before and after thermal treatments was not detected. The XRD results indicate the formation of more than one phase. Only one peak is observed at $2\theta = 43.7^\circ$, which correlates mainly to (111) fcc copper. However, there is a slight shift towards high angles for the (111) reflections with increasing annealing time and consequently a slight decrease in the d-spacing. Another weak reflection at $2\theta = 41.6^\circ$ appeared. This reflection may correspond to a hcp cobalt phase ($(10\bar{1}0)$ planes) and/or to a tungsten contamination in the copper X-ray tube. It is known that electrodeposition of cobalt from a solution at pH above 2.9 results mainly in a hcp cobalt [35, 39, 40]. The deposition of Cu-Co alloys was conducted at pH 6–6.5, clearly above 2.9; therefore, the formation of hcp cobalt is possible. Since the hcp cobalt reflection is not absolute and other characterization tools cannot verify the existence of hcp cobalt, grain size estimation of the hcp phase was not possible. The (111) reflection was deconvoluted to two (111) reflections of fcc copper and cobalt. The values for the average fcc cobalt grain calculated using the XRD reflections are listed in Table I. As expected, there is grain growth with annealing time.

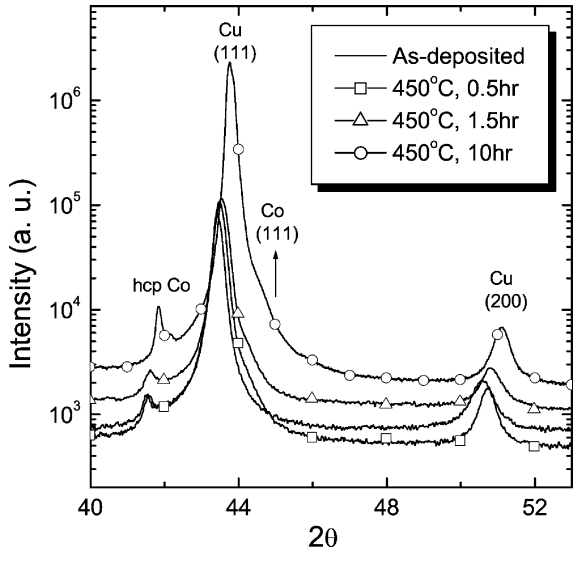

Figure 1 XRD of Cu-Co films before and after sequences of thermal treatments. There is no indication of evolution of a new fcc cobalt phase, only a slight shift towards high angles for the (111) reflections with increasing annealing time.

3.2. AES

Auger surface composition and depth profile analysis was performed on as-deposited Cu-Co films as a function of the electrodeposition parameters; substrate type (Cu/Co), thickness variation and agitation, in order to examine whether the copper deposition process is mass transfer limited. A full description of the AES results on as-deposited Cu-Co films without agitation on a copper substrate is published elsewhere [35]. AES depth profile analysis indicated that the as-deposited Cu-Co film is inhomogeneous independent of the substrate type and film thickness; the bulk of the film is richer in Co while the surface and bottom of the film are Co-poor. Fig. 2 presents the depth profile analysis of a as-deposited Cu-Co film, deposited using agitation. The Auger peaks were computer differentiated and the peak-to-peak area values for Cu, Co and oxygen were used together with the EDS results to determine the atomic concentrations presented in Fig. 2. When the electrodeposition process is assisted by agitation, a high content of oxygen and a lower Co concentration is found. The rise in oxygen towards the surface indicated the oxidation of the deposit. This corresponds to the sharp decrease in copper and cobalt at the surface. The concentration profile of Co declines during the deposition process, especially, toward the final stages of the process (inset in Fig. 2). The homogeneity of the film was not improved, but

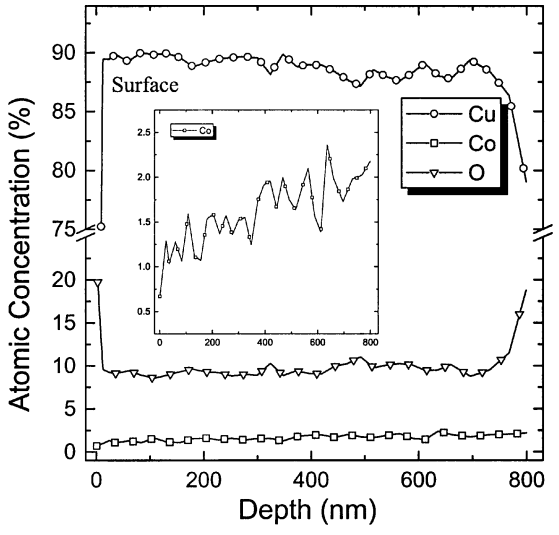

Figure 2 AES depth-profile of a Cu-Co film as-deposited on a Cu substrate with agitation, a Cu-Co film with an extensively reduced Co concentration was formed, and a relatively stable concentration profile of Cu with a small rise toward the final stages of the deposition process. Inset: Larger magnification of Co depth profile, the concentration profile of Co declines during the deposition process, especially, toward the final stages of the process.

the concentration profile of Cu was more stable with a small rise toward the final stages of the deposition process. The high content of oxygen inside the film that was formed under agitation probably indicates porosity, where the deposit is oxidized after the deposition. The use of agitation (Fig. 2), probably caused bubbles in the plating solution that partly blocked the deposition and thus a porous deposit was formed. In addition, an inhomogeneous film was formed when the sample was removed from the solution before the polarization was stopped.

3.3. TEM

Fig. 3 presents the energy-filtered bright field (BF) TEM micrographs (elastically scattered electrons) of the samples annealed for 30 min and 10 h. As expected, it is not possible to distinguish between copper and cobalt grains, even after long durations of annealing (10 h). However, the microstructure of the Cu-Co alloys was revealed by the ESI images showing elemental maps of Cu (red), Co (green) and Oxygen (blue) (Fig. 4). The ESI results from the as-deposited film (Fig. 4a and b) support the scanning Auger microprobe analysis (AES) [35] indicating an inhomogeneous film; the bulk part of the film is richer in Co while the surface and bottom of the film are Co-poor. According to the elemental maps from the ESI analysis, there is a ∼90 nm thick copper underlayer with traces of oxygen, and a ∼30 nm thick copper overlayer. The bulk of the film is composed of metastable Cu-Co, Cu and Co phases. There are regions of color combinations of the two elements Co and Cu (yellow), which are very homogeneous in intensity. The pure cobalt regions appear as a coalescence of Co grains, and nano grains that are too small to be quantitatively measured (∼1 nm) (Fig. 4). The elemental maps of Cu and Co support the XRD results that the as-deposited film is composed of more than one phase; a solid solution of Cu-Co phase and pure Cu and Co phases.

After sequences of thermal treatments, voids formed in the PVD copper layer, and there is an indication of cobalt precipitation and/or evolution of a new cobalt phase (Fig. 4c–f). More cobalt grains appear with a larger grain size as the annealing time increases. After annealing at 450°C for 30 min, one can still observe a smaller metastable region, a coalescence of Co grains, and that the Co particle distribution is not uniform along the film depth (Fig. 4c). The cobalt grains further grow with annealing time, and the distribution of the Co grains is more uniform (Fig. 4d and e). A thin film of cobalt of less than 1 nm is observed under the PVD copper substrate and above the TaN layer, which is a diffusion barrier (Fig. 4f). The average cobalt grain size, which ranges from 1 to ∼40 nm is listed in Table I.

3.4. Magnetic measurements

The resistivity measurements were made with a magnetic field parallel and perpendicular to the sample, on as-deposited Cu-Co alloys and after various annealing

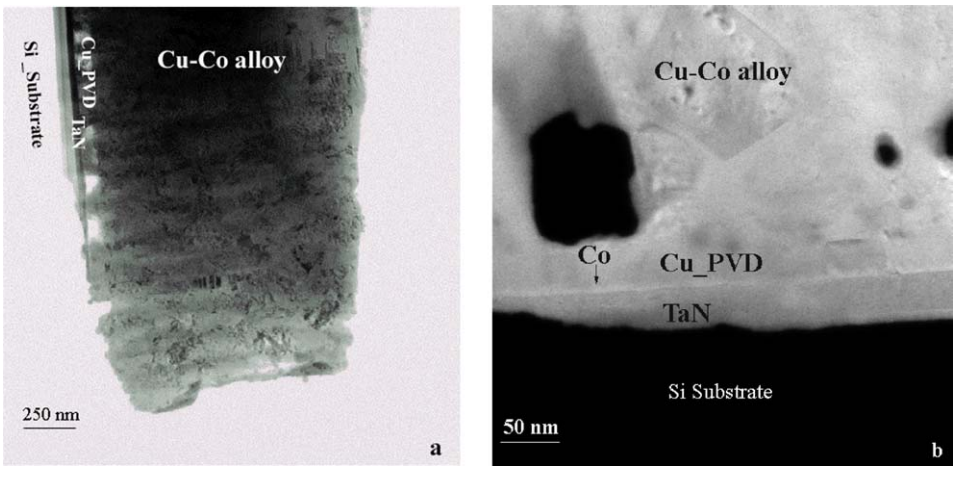

Figure 3 Zero loss filtered bright field TEM micrographs of a heterogeneous Cu-Co alloy formed by electrodeposition (cross-section view). (a) annealed at 450°C for 30 min. (b) annealed at 450°C for 10 h. No distinction between copper and cobalt was possible, even after long duration of annealing (10 h).

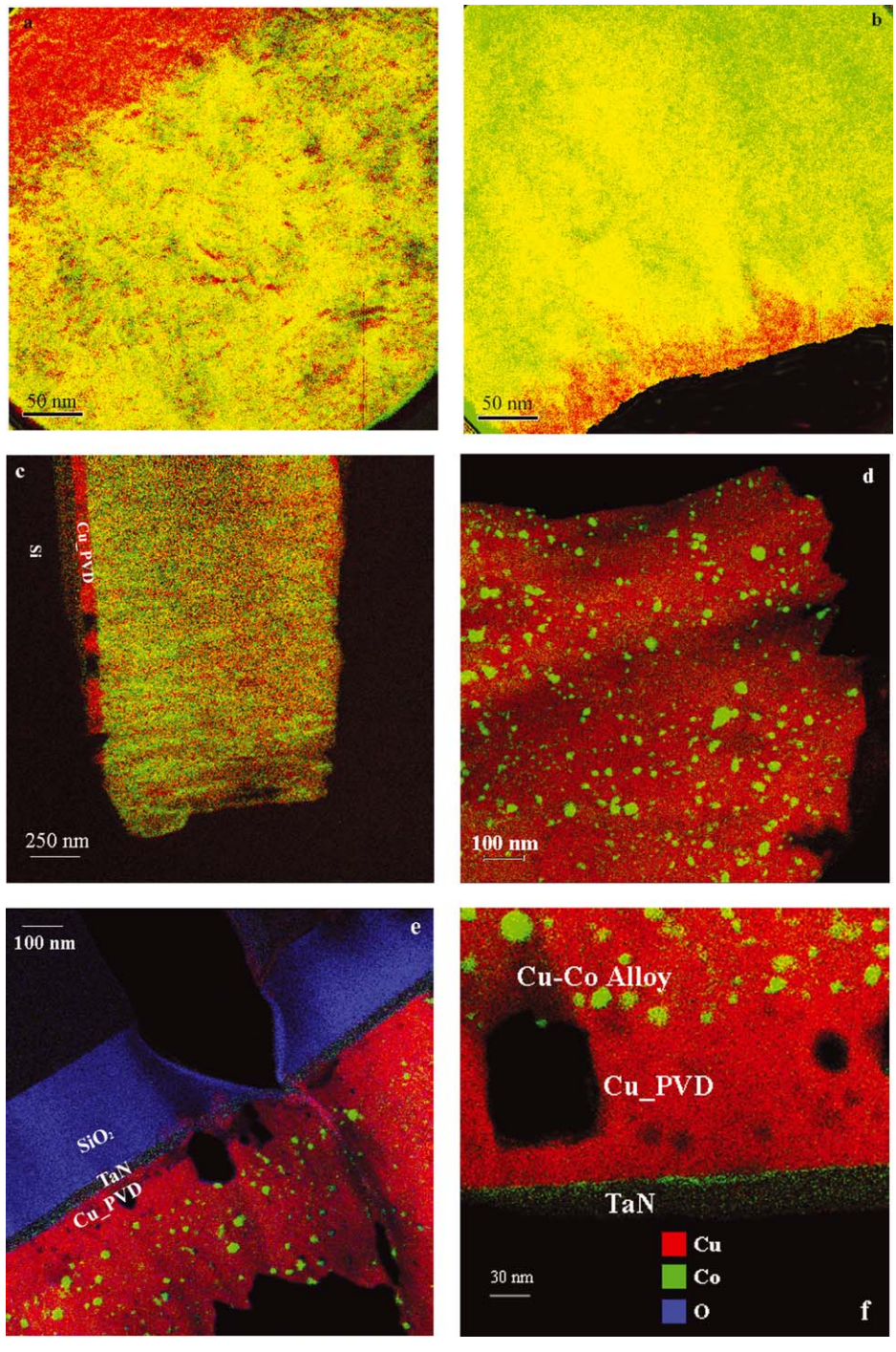

Figure 4 Elemental maps of heterogeneous Cu-Co alloy for copper (red), cobalt (green) and oxygen (blue) in a false color image (cross-section view). (a) bottom of the as-deposited Cu-Co film, (b) bulk and upper parts of the Cu-Co film, (c) annealed at 450°C for 30 min, (d) annealed at 450°C for 90 min and (e and f) annealed at 450°C for 10 h.

treatments. The results are shown in Fig. 5. No influence of the field position was observed, indicating that the cobalt grains are isotropic. Surprisingly, the as-deposited Cu-Co alloy also exhibited a non-negligible GMR effect of 2% at 273 K and 7% at 5 K. In addition, no saturation in the resistivity behavior was achieved up to a field of 7.5 T in the as-deposited films. The MR ratio exhibited a peak behavior; a maximum GMR effect of 15% at 5 K and 5% at 273 K was measured after 1.5 h at 450°C. The GMR effect decreased and saturation was achieved at a lower field, IT, after annealing for 10 h. The Cu-Co films exhibited ferromagnetic characteristics at $T \leq 298$ K; a magnetic saturation and hysteresis behavior was observed in all the samples.

4. Discussion

The as-deposited Cu-Co films are inhomogeneous according to AES, XRD and ESI analysis; the bulk of the film is richer in Co while the surface and bottom of the film are Co-poor. According to AES depth profile analysis, the inhomogeneity of these films is independent of the substrate type (Cu or Co) and the thickness of the films. The elemental maps of Cu and Co (Fig. 4) revealed the existence of at least three phases in the as-deposited film and support the XRD analysis that the as-deposited film is composed of more than one phase; fcc copper, a fcc solid solution of Cu-Co phase and a Co phase. The GMR behavior of the as-deposited films indicates that there are small superparamagnetic cobalt

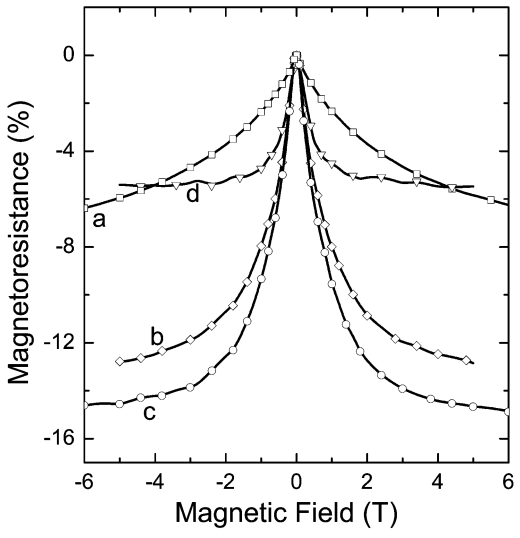

Figure 5 Field dependent GMR effect for Cu-Co films as-deposited (a) and for different annealing treatments at 450°C, measured at 5 K. b (0.5 h), c (1.5 h), d (10 h). A maximum GMR effect was found after annealing at 450°C for 1.5 h.

grains, since no saturation in the as-deposited film was achieved up to 7.5T (Fig. 5). A comparison of the characterization results with the resistivity measurements indicates that the SP behavior is probably due to the pure Co phase.

The large difference between the polarization of Cu and Co may be the cause of the inhomogeneity of the film. Since copper is nobler than cobalt, the deposition rate of Co is negligible compared to Cu during the initial stages of the deposition process, despite the higher Co bath concentration and a larger diffusion coefficient of cobalt in the deposition bath [41, 42]. This can be explained by the high *over-potential* for the deposition of cobalt on copper. The copper deposition rate becomes diffusion limited with the advance of the plating process, which enables a relatively higher cobalt deposition rate. When a higher deposition rate of cobalt becomes possible, a metastable solution of Cu–Co is formed in the *over-potential* regime. Electrodeposition in a high *over-potential* regime may result in metastable phases [43]. When the electrodeposition process is assisted by agitation, a Cu-Co film with a lower Co concentration is formed, and the concentration profile of Cu was more stable, with a small rise towards the final stages of the deposition process (Fig. 2). This proves that the copper deposition process is mass transfer limited, and this results in an inhomogeneous film. STM results [35] showed that faceting appears when these two elements are deposited together, due to strain relief during the deposition process, and this can lead to the precipitation of cobalt. This means that the solubility threshold of Co in metastable Cu-Co alloys formed by electrodeposition is lower (less than ∼7.5 at.%) than that formed by physical deposition methods (∼35%) [23]. The mechanism for the lower solubility limit in a non-equilibrium electrodeposition process will be the focus of a further study. The reason for a copper over-layer is a chemical exchange process between the copper ions in the solution and cobalt atoms in the alloy [35]. The decline in the concentration profile of Co towards the final stages of the deposition process, when agitation was used, is due to the higher limiting current for copper deposition.

An inhomogeneous Cu-Co film, a lower solubility limit of Co in the metastable structure, and the coalescence microstructure of Co grains may reduce the GMR effect by causing magnetic interactions (Fig. 4a–c). Magnetic interactions may effectively increase the grain size via a coupling mechanism between the Co grains, i.e., ferromagnetic coupling may result between two Co grains, which are physically separate, and thus the magnetic behavior of a single particle is formed. After annealing for 90 min a more homogeneous dispersion of Co grains in the Cu matrix resulted in a maximum GMR effect of 15% (at 5 K) (Fig. 4d). The GMR effect is related to spin-dependent scattering of conduction electrons within the magnetic grains, and to a larger extent at the interfaces between the magnetic grains and non-magnetic media [18]. Two processes occurred during annealing; there is grain growth of the as-deposited cobalt phase and precipitation of new fcc cobalt grains from the metastable phase. The scattering effect is increased by the precipitation of Co grains, and reduced by grain growth of the as-deposited Co phase. The decrease in the GMR effect with annealing time (after 90 min) is due to Co grain growth. Grain growth reduces the surface-to-volume ratios, which leads to the formation of multi-magnetic domains in the Co grains instead of a single domain, and the grain size becomes larger than the mean free path of the electrons.

It seems that as a consequence of long thermal treatments cobalt diffuses away from the metastable phase to the edges of the Cu-Co film, until it is blocked by the surface of the film or the diffusion barrier (TaN at the substrate) (Fig. 4f). ESI results support the equilibrium phase diagrams and indicate that there is little or no solubility between copper and cobalt up to 450°C. The diffusion coefficient of cobalt in pure copper is 1.46×10^{-16} cm^2/s or 0.0146 nm^2/s at 450°C [44], meaning that it is possible for cobalt atoms to diffuse from the metastable film and reach the TaN barrier after 10 h at 450°C.

The Bragg-Brentano XRD and the ESI method (which was conducted on cross-section samples) provide information on the grain size in the axis perpendicular to the surface of the specimen. Thus, the comparison of the grain-size measured from thin Cu-Co films by these two methods is appropriate. One should note that the accuracy of the cobalt grain size measurements from the ESI images is limited. No distinction between clusters of small Co grains and large Co grains is possible. Since the characterization was conducted on cross-section samples, the shape and size of the Co grains are not absolute. Given this, the *estimation* of the grain size from TEM agrees with the XRD and magnetization grain size measurements results (Table I).

In non-interacting predominately superparamagnetic magnetic grains, there should be a quadratic dependence of the relative resistance changes ($\Delta R/\Delta R$) on the magnetization (M) of the samples [45]. Fig. 6 presents the dependence of the magnetoresistance on the normalized magnetization of the different samples. Only the results from the as-deposited film fits

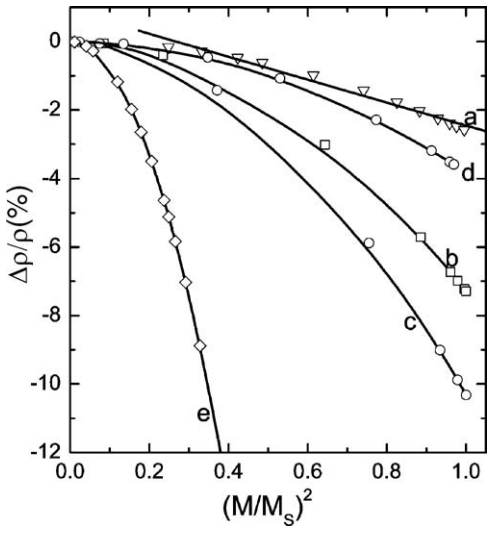

Figure 6 GMR effect as a function of the normalized magnetization of the different samples. Only the results of the as-deposited (a) film fits the theoretical model, while the samples annealed at 450°C (b: 0.5 h, c: 1.5 h, d: 10 h) exhibit a significant deviation from the quadratic behavior (flat-top parabola), especially at low field regions (at $M/M_s \approx 0$).

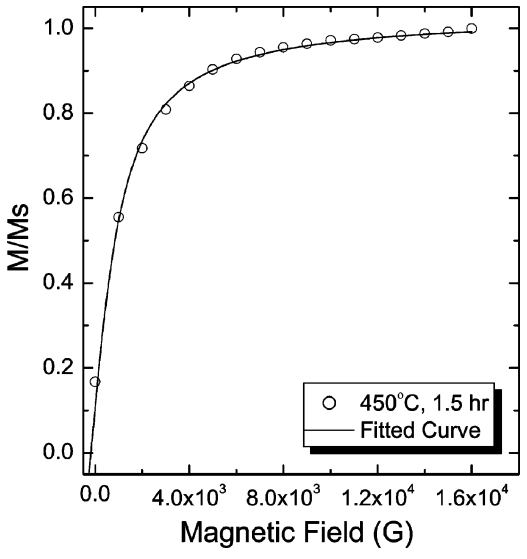

Figure 7 Normalized magnetization of a Cu-Co alloy annealed at 450°C for 1.5 h. Circles: experimental data, full line: best fit according to Equation 2.

the theoretical model, while the annealed samples exhibit a significant deviation from the quadratic behavior (flat-top parabola), especially in low field regions (at $M/M_s \approx 0$). The deviation from this model is not an exception and has been reported frequently [18, 46–48]. A number of explanations for this deviation from quadratic behavior were proposed, including; grain size distribution [45–47], alignment of the disordered surface spins under high magnetic fields [49], the interaction effects between the magnetic grains [46, 50, 51] and the presence of different magnetic phases. As was shown from the ESI analysis there is a wide grain size distribution, more than one magnetic phase in the annealed samples, and magnetic interactions between the Co grains are possible. In addition, one can not exclude the existence of size and shape dispersions of the Co grains in the Cu-Co film. Both SP and FM grains of cobalt may exist in the annealed samples. However, all the samples exhibited a FM behavior, hysteresis loops and saturation at ∼1T. The source of the coercivity can result from FM grains, from interactions between SP grains, or from the existence of SP grains with a blocking temperature above 300 K [18]. Since the coercivity decreases slightly with increasing temperature of the measurements, one can assume that the coercivity originates mainly from the FM phase. If the electrodeposited Cu-Co film is composed of two different magnetic phases, SP and FM, then the magnetization of the annealed films will be a function of these two phases [53]:

$$M_T(H) = \frac{2M_{FM}^s}{\pi}\tan^{-1}\left[\frac{H \pm H_C)}{H_C}\tan\left(\frac{\pi S}{2}\right)\right] + N_g\bar{\mu}\left[\mathrm{ctnh}\left(\frac{\bar{\mu}H}{kT}\right) - \left(\frac{\bar{\mu}H}{kT}\right)^{-1}\right] \quad (2)$$

The first term describes the FM hysteresis curve and the second term describes SP behavior. M_{FM}^s and $M_{SP}^s = N_g\bar{\mu}$ is the saturation magnetization of the FM and SP components. S is the squareness of the ferromagnetic loop, i.e., the ratio of the remanent magnetization, M_R, to $M_{FM}^s \cdot \bar{\mu}$ is the average moment per grain and N_g is the number of Co grains/cm^3 in the SP component.

Using equation 2, the fitted curves (obtained using a non-linear fitting procedure) are consistent with the experimental magnetization curves (Fig. 7). The average diameter of the Co grains and the fraction of the SP phase calculated from the fitting analysis are listed in Table I. A dominant FM phase appeared in all the Cu-Co films. The fraction of the SP phase increases after annealing for 30 min, indicating the precipitation of small Co grains. However, as was shown in the ESI images, there is coalescence of Co grains and this is the reason the FM phase is still dominant (Fig. 4c). The amount of the SP phase became negligible after annealing for more than 30 min (less than 8%). In addition, zero-field cooled and field cooled dc susceptibility experiments on all of the Cu-Co samples did not exhibit a blocking temperature. The critical size of transition from SP to FM states at room temperature is ∼17 nm for a fcc Co particle, while it is ∼7 nm for a hcp Co particle [54]. Co particles in the Cu-Co films with a mean diameter of less than 17 and 10 nm (Table I) exhibit ferromagnetic behavior with a small hysteresis at 298 K. This is probably caused by magnetic interactions between the grains, as seen in the ESI images (Fig. 4).

A clear description of the microstructure of cobalt in the as-deposited and annealed films is given by ESI analysis. ESI indicates without doubt the existence of a metastable phase of Cu-Co in the as-deposited film, compared to other characterization methods such as conventional TEM, XRD and magnetization measurements. The elemental maps from the ESI analysis support the optimal annealing time for achieving the highest GMR effect, and indicate a low solubility threshold of Co in the metastable phase, and that a significant fraction of the cobalt in the Cu-Co film does not contribute to the GMR effect. Prior to this optimal annealing time

the Co grains are close to each other, such that magnetic interactions between the magnetic grains occur, the amount of SP grains is still considerable, and more Co grains can precipitate from the metastable state. Beyond the optimum annealing time, the distribution of FM grains is more homogeneous in the film, but most of the FM grains are too large, the ratio of surface to volume decrease, more multi-domains are formed, and spin-dependent scattering is diminished. To our knowledge, this is the first time that the evolution of cobalt precipitates from a metastable Cu-Co phase has been revealed by ESI analysis.

5. Summary and conclusions

The microstructure, magnetic properties and GMR of Cu-Co films [Cu92.5-Co7.5] (at.%) prepared by electrodeposition were studied. By combinating of ESI and resistivity measurements, optimization of the fabrication of heterogeneous alloys for GMR application is possible.

The as-deposited film is composed of more than one phase; fcc copper, metastable fcc Cu-Co and cobalt. The granular microstructure is extremely complex, including the coexistence and interaction of SP and FM grains of cobalt. The FM behavior is dominant, independent of annealing, due to the inhomogeneity of the as-deposited Cu-Co films and grain growth which occurs after extended annealing. During annealing, the metastable phase decomposes into two fcc phases; Cu and Co. Grain growth occurs with increasing annealing duration, and the Co grains are more homogeneously distributed in the Cu matrix. A maximum GMR effect was formed after annealing at 450°C for 1.5 h, which corresponds to an average cobalt grain size of 5.5 nm according to magnetization characterization.

It seems that a significant fraction of the cobalt in the Cu-Co film does not contribute to the GMR effect due to interactions between the different magnetic grains and large FM grains. The solubility threshold of Co in metastable Cu-Co alloys formed by electrodeposition is lower (less than ∼7.5 at.%) than that prepared by physical methods (∼35 at.%).

References

1. M. N. BAIBICH, J. M. BROTO, A. FERT, F. NGUYEN VAN DAU, F. PETROFF, P. ETIENNE, G. CREUSET, A. FRIEDERICH and J. CHAZELAS, *Phys. Rev. Lett.* **61** (1988) 2472.
2. W. SCHWARZACHER and D. S. LASHMORE, *IEEE Trans. Magn.* **32** (1996) 3133.
3. S. ZHANG, *Appl. Phys. Lett.* **61** (1992) 1855.
4. S. ZHANG and P. M. LEVY, *J. Appl. Phys.* **73** (1993) 5315.
5. K. YAMAMOTO and M. KITADA, *Thin. Solid Films* **263** (1995) 111.
6. A. E. BERKOVITZ, J. R. MITCHELL, M. J. CAREY, A. P. YOUNG, F. E. SPADA, F. T. PARKER, A. HÜTTEN and G. TOMAS, *Phys. Rev. Lett.* **68** (1992) 3745.
7. J. Q. XIAO, J. S. JIANG and C. L.CHIEN, *ibid.* **68** (1992) 3749.
8. J. YAHALOM and O. ZADOK, *J. Mater. Sci.* **21** (1987) 499.
9. H. J. BLYTHE and V. M. FEDOSYUK, *Phys. Stat. Sol.* (a) **146** (1994) K13.
10. O. F. BAKKALOGLU, I. H. KARAHAN, H. EFEOGLU, M. YILDIRIM, U. CEVIK and Y. K. YOGURTCU, *J. Magn. Magn. Mater.* **197** (1998) 53.
11. H. ZAMAN, A. YAMADA, H. FUKUDA and Y. UEDA, *J. Electrochem. Soc.* **145** (1998) 565.
12. P. E. BRADLEY and D. LANDLOT, *Electrochim. Acta* **45** (1999) 1077.
13. K. MIYAZAKI, S. KAINUMA, K. HISATAKE, T. WATANABE and N. FUKUMURO, *ibid.* **44**(21/22) (1999) 3713.
14. S. H. GE, H. H. LI, C. LI, L. XI, W. LI and J. CHI, *J. Phys.: Condens. Matter* **12** (2000) 5905.
15. G. R. PATTANAIK, S. C. KASHYAP and D. K. PANDYA, *J. Magn. Magn. Mater.* **219** (2000) 309.
16. E. GÓMEZ, A. LABERTA, A. LLORENTE and E. VALLÉZ, *J. Electroanal. Chem.* **517** (2001) 63.
17. R. LÓPEZ, J. HERREROS, A. GARĆIA-ARRIBAS, J. M. BARANDIARÁN and M. L. FDEZ-GUBIEDA, *J. Magn. Magn. Mater.* **196–197** (1999) 53.
18. M. KUŹMIŃSKI, A. ŚLAWSKA-WANIEWSKA, H. K. LACHOWICZ and M. KNOBEL, *ibid.* **205** (1999) 7.
19. G. L. ZHOU, M. H. YANG and C. P. FLYNN, *Phys. Rev. Lett.* **77** (1996) 4580.
20. M. A. HOWSON, S. O. MUSA, M. J. WALKER, B. J. HICKEY, R. COCHRANE and R. STEVENS, *J. Appl, Phys.* **75**(10) (1994) 6546.
21. O. I. KASYUTICH, T. A. TOCHITSKII and V. M. FEDOSYUK, *Phys. Stat. Sol.* (a) **162** (1997) 631.
22. X. SONG, S. W. MAHON. R. F. COCHRANE, B. J. HICKEY and M. A. HOWSON, *Matt. Lett.* **31**, (1997) 261.
23. A. N. POHORILYI, A. F. KRAVETZ, E. V. SHIPIL, A. YA. VOVK, CHANG SIK KIM and H. R. KHAN, *J. Magn. Magn. Mater.* **186** (1998) 87.
24. W. WANG, F. ZHU, W. LAI, J. WANG, G. YANG, J. ZHU and Z. ZHANG, *J. Phys. D: Appl. Phys.* **32** (1999) 1990.
25. G. Y. YANGA, JING ZHU, W. D. WANG, Z. ZHANG and F. W. ZHU, *Mater. Res. Bull.* **35** (2000) 875.
26. J. J. KELLY, M. CANTONI and D. LANDOLT, *J. Electrochem. Soc.* **148** (2001) C620.
27. T. A. TOCHITSKII, G. A. JONES, H. J. BLYTHE, V. M. FEDOSYUK and J. CASTRO, *J. Magn. Magn. Mater.* **224** (2001) 221.
28. H. ERRAHMANI, A. BERRADA, G. SCHMERBER and A. DINIA, *ibid.* **238** (2002) 145.
29. G. R. PATTANAIK, D. K. PANDYA and S. C. KASHYAP, *J. Electrochem. Soc.* **149** (2002) C363.
30. L. BALCELLS, A. HÜTTEN, J. BERNARDI, S. FRIEDRICHS and G. THOMAS, *Scripta Metall. Mater.* **33** (1995) 1647.
31. F. HOFER, P. WARBICHLER and W. GROGGER, *Ultramicroscopy* **59** (1995) 15.
32. J. M. PLITZKO and J. MAYER, *ibid.* **78** (1999) 207.
33. F. HOFER, W. GROGGER, G. KOTHLEITNER and P. WARBICHLER, *ibid.* **67** (1997) 83.
34. J. MAYER and J. M. PLITZKO, *J. Microsc.* **183**(1) (1996) 2.
35. T. COHEN-HYAMS, W. D. KAPLAN, D. AURBACH, Y. S. COHEN and J. YAHALOM, *J. Electrochem. Soc.* **150**(1) (2003) C28.
36. TH. H. DE KEIJSER, J. I. LANGFORD, E. J. MITTEMEIJER and A. B. P. VOGELS, *J. Appl. Cryst.* **15** (1982) 308.
37. S. KRUMN, WinFit 1.2.1, http://dxray.mpi-stuttgart.mpg.de/site/software/mfintro_en.html.
38. I. T. WALKER, Department of Materials Science & Metallurgy, University of Cambridge, Pembroke Street, Cambridge. http://ccp14.semo.edu/ccp/web-mirrors/bca-spreadsheets/Snglinesizstrn.xls
39. J. W. DINI, in "Electrodeposition" (Noyes, 1993) p. 156.
40. S. NAKAHARA and S. MAHAJAN, *J. Electrochem. Soc.* **127** (1982) 283.
41. S. F. PATIL, A. V. BORHADE and M. NATH, *Appl. Radiat. Isot.* **45** (1994) 1.
42. C. SCHÖNENBERGER, B. M. I. VAN DER ZANDE, L. G. J. FOKKINK, M. HENNY, C. SCHMID, M.

KRULGER, A. BACHTOLD, R. HUBER, H. BIRK and U. STAUFER, *J. Phys. Chem.* B **101** (1997) 5497.
43. M. PAUNOVIC and M. SCHLESINGER, "Fundamentals of Electrochemical Deposition," (John Wiley & Sons, New York, 1998) p. 188.
44. R. DÖHL, M.-P. MACHT and V. NAUNDORF, *Phys. Stat. Sol.* A **86** (1984) 603.
45. J. Q. XIAO, J. S. JIANG and C. L. CHIEN, *Phys. Rev.* B **46**(14) (1992) 9266.
46. P. ALLIA, M. KNOBEL, P. TIBERTO and F. VINAI, *ibid.* B **52**(21) (1995) 15398.
47. S. ZHANG and P. M. LEVY, *J. Appl. Phys.* **73** (1993) 5315.
48. E. F. FERRARI, F. C. S. DA SILVA and M. KNOBEL, *Phys. Rev.* B **56**(10) (1997) 6086.
49. C. BELLOURAD, B. GEORGE and G. MARCHAL, *J. Phys.: Condens. Mater.* **6** (1994) 7239.
50. J. F. GREGG, S. M. THOMPSON, S. J. DAWSON, K. OUNADJELA, C. R. STADDON, J. HAMMAN, C. FERMON, G. SAUX and K. O'GRADY, *Phys. Rev.* B **49** (1994) 1064.
51. M. EL-HILO, K. O'GRADY and R. W. CHANTRELL, *J. Appl. Phys.* **76** (1994) 6811.
52. A. D. C. VIEGAS, J. GESHEV, L. S. DORNELES, J. E. SCHMIDT and M. KNOBEL, *ibid.* **82** (1997) 3047.
53. M. B. STEARNS and Y. CHENG, *ibid.* **75** (1994) 6894.
54. O. KITAKAMI, T. SAKURAI, Y. MIYASHITA, Y. TAKENO, Y. SHIMADA, H. TAKANO, H. AWANO, K. ANDO and Y. SUGITA, *Jpn. J. Appl. Phys.* **35** (1996) 1724.

Received 15 September 2003
and accepted 11 May 2004